Robustness of helical hinge states of weak second-order topological insulators

C. Wang [1,*] and X. R. Wang [2,3,†]

[1]*Center for Joint Quantum Studies and Department of Physics, School of Science, Tianjin University, Tianjin 300350, China*
[2]*Physics Department, The Hong Kong University of Science and Technology (HKUST), Clear Water Bay, Kowloon, Hong Kong*
[3]*HKUST Shenzhen Research Institute, Shenzhen 518057, China*

(Received 4 September 2020; revised 8 February 2021; accepted 25 February 2021; published 11 March 2021)

Robustness of helical hinge states of three-dimensional weak second-order topological insulators (WSOTIs) against disorders is studied. The pure WSOTI is obtained from a weak $\mathbb{Z}_2$ first-order topological insulator through a surface band inversion. Both bulk states and surface states in the WSOTI are gapped, and in-gap valley-momentum locked helical hinge states are topologically protected by the surface valley-Chern number. In the presence of weak disorders, helical hinge states are robust against disorders while the quantized conductance of the states is fragile due to the intervalley scattering. As disorder increases, the system undergoes a series of quantum phase transitions: from the WSOTI to the weak first-order topological insulator, then to a diffusive metal and finally to an Anderson insulator. Our results thus fully establish the WSOTI phase as a genuine state of matters and open a door for the second-order valleytronics that allows one to control the valley degree of freedom through helical hinge states.

DOI: 10.1103/PhysRevB.103.115118

I. INTRODUCTION

Topological insulators (TIs) characterized by topological invariants and robust boundary states have attracted great interest because of their exotic properties. The band inversion resulting in nonzero Chern numbers of a band is the central theme of topological materials. The nonzero topological invariants give rise to a bulk-boundary correspondence and the necessity of gapless boundary states in the band gap. The standard paradigm of the first-order TIs (FOTIs) claims that a d-dimensional insulator with band inversion has $(d-1)$-dimensional in-gap boundary states [1–10]. In three dimensions (3D), FOTIs are strong (weak) when the number of surface Dirac cones is odd (even). In the presence of the time-reversal symmetry, a weak FOTI (WFOTI) has zero principle $\mathbb{Z}_2$ index ν_0, at least one nonzero weak index (ν_1, ν_2, ν_3), and an even number of Dirac cones on surfaces not perpendicular to (ν_1, ν_2, ν_3). With this understanding of FOTIs, most recent activities have been focused on higher-order TIs with a generalized bulk-boundary correspondence [11–33]. The new paradigm is that, with band inversions on a d-dimensional manifold and its submanifolds, gapped bands in the manifold and its submanifolds of dimensions larger than $d-n$ can have gapless states in a boundary submanifold of dimension $d-n$. For example, a 3D second-order TI has gapless states on the sample hinges inside its bulk and surface band gaps [12,14–16,18,19,22]. These hinge states have been predicted and observed in real materials, e.g., bismuth crystals [34] and magnetic axion insulator $Bi_{2-x}Sm_xSe_3$ [35].

As a well-accepted paradigm, hinge states appear at the intersections of two surfaces of different topological classes when the surface Dirac cones of a 3D FOTI are gapped. Hinge states could be either chiral [14] or helical [15,16,19,22], depending on whether the number of surface Dirac cones is odd or even. Robustness of those states against disorders is a fundamental issue because disorders exist inevitably in all materials and hinge states must survive in disorders in order to be a genuine state. Chiral hinge states can survive in random media due to the absence of backward scattering [36], while inter-spin/valley scatterings are allowed in helical hinge states and may result in the disappearance of these states through Anderson localizations at an infinitesimally weak disorder. The occurrence of this scenario, however, contradicts a general belief that the in-gap hinge states should persist at finite disorders until the surface state gap closes [37–39]. Hence, whether disorder-induced backward scatterings can destroy the helical hinge states is not clear and should be examined.

In this work, we report a weak second-order TI (WSOTI) generated from a WFOTI with a time-reversal-like symmetry through band inversion of its surface states. Different from other reported helical hinge states [15,16,19,22] that lock the momentum with spins, carriers in different valleys of WSOTIs move to the opposite directions along a hinge. In clean cases, such helical hinge states are characterized by the quantized valley-Chern number. They survive in the presence of weak but finite disorders, similar to the surface states in WFOTIs. Helical hinge states can be identified by the dominate occupation probability on hinges and negligible occupation probability in the bulks and on the surfaces. With increasing disorders, a gap-closing transition from WSOTI to WFOTI happens at a critical disorder W_{c1} at which gaps of surface Dirac cones close. Moreover, with further increasing disorders from W_{c1}, the WFOTI becomes a diffusive metal (DM) and finally an Anderson insulator (AI). Electronic transport through helical hinge states is also studied. We find that the quantum resistance is the sum of an intrinsic contribution from

*Corresponding author: physcwang@tju.edu.cn
†Corresponding author: phxwan@ust.hk

the topological states and an extrinsic part from the intervalley scatterings that is proportional to system sizes. These results cast the authenticity of helical hinge states that provide a way to manipulate the valley degree of freedom.

The paper is organized as follows: In Sec. II, we demonstrate the model of the WSOTI in the clean limit and show that helical hinge states in clean WSOTIs can be characterized by the quantized valley-Chern number. Through two independent numerical approaches, we substantiate the robustness of the helical hinge states against weak disorders in Sec. III. The electronic transport through helical hinge states is studied in Sec. IV. In Sec. V, we elaborate a phase diagram of the WSOTI in the presence of strong disorders, and a summary is given in Sec. VI.

II. CLEAN WSOTI

A clean WSOTI can be modelled by the following Hamiltonian in the momentum space

$$h_{\text{bulk}}(\boldsymbol{k}) = t\sin k_2\Gamma^1 + (M - t(\cos k_2 + \cos k_3))\Gamma^2 + t\sin k_3\Gamma^3 + t\sin k_1\Gamma^4 + B\Gamma^{31}. \quad (1)$$

Here, $\Gamma^{\mu=1,2,3,4,5} = (s_1\otimes\sigma_1, s_2\otimes\sigma_1, s_3\otimes\sigma_1, I_2\otimes\sigma_3, I_2\otimes\sigma_2)$ are the four-by-four nonunique gamma matrices with s_μ and σ_μ being the Pauli matrices acting on spin and orbital spaces, respectively. $I_{\mathcal{D}}$ is the identity matrix of dimension $\mathcal{D}$. Hopping energy $t = 1$ is chosen as the energy unit. Equation (1) is invariant under the reflection symmetry of $\Pi = (I_2\otimes\sigma_1)$ such that $\Pi h(k_1, k_2, k_3)\Pi = h(-k_1, k_2, k_3)$. Beside the reflection symmetry, our model of $B = 0$ has a time-reversal-like symmetry. This can be clearly seen from the commentator of $\Theta = -i(I_2\otimes\sigma_2)K$ with the Hamiltonian. Here, I_2 is the two-by-two identity matrix acting on the spin space (a reason for Θ called time-reversal-like operator, instead of time-reversal operator) and K is the complex conjugation operation, such that $\Theta^2 = -1$ and $\Theta^{-1} = -\Theta$. For $B = 0$ and $M \in (0, 2)$, Eq. (1) is a WFOTI that can be characterized by the $\mathbb{Z}_2$ indexes $(\nu_0, \nu_1\nu_2\nu_3) = (0, 001)$ [40–42]. Such a $\mathbb{Z}_2$ index guarantees two Dirac cones on the surfaces not perpendicular to the vector (0,0,1), e.g., yz facets. For $B > 0$, the last term within the surface state subspace acts like an effective Dirac mass [14]. To see it, we derive the low-energy effective Hamiltonian of the surface Dirac cones on the yz facets with open boundary condition (OBC) applied in the x direction. The effective Hamiltonian, expanded around two Dirac cones (valleys) $\boldsymbol{K} = (0, 0)$ and $\boldsymbol{K}' = (\pm\pi, \pm\pi)$, reads (see Appendix A for a detailed derivation)

$$h_{\text{surface}}(\boldsymbol{p}_\parallel = (p_2, p_3)) = \begin{bmatrix} h_{\mathbb{S}}(\boldsymbol{p}_\parallel) & 0 \\ 0 & \mathcal{T}h_{\mathbb{S}}(\boldsymbol{p}_\parallel)\mathcal{T}^{-1} \end{bmatrix} \quad (2)$$

with $h_{\mathbb{S}}(\boldsymbol{p}_\parallel) = tp_2\tau_1 + tp_3\tau_3 + (B - t'^2p_2^2/2)\tau_2$. $\tau_{1,2,3}$ are the Pauli matrices in the basis of the zero-energy surface states wave functions. The upper and lower blocks are for $\boldsymbol{K}$ and $\boldsymbol{K}'$ related by the pseudo-time-reversal symmetry represented by $\mathcal{T} = -i\tau_2K$. In what follows, we denote $\boldsymbol{K}$ and $\boldsymbol{K}'$ by $\eta_i = \pm 1$. If the two facets are separated by a distance, the Newton mass t' decays exponentially with the distance such that the band inversion is prevented, while if they meet at the reflection plane of $x = 0$, $t' = t/2$. Equation (2) has been

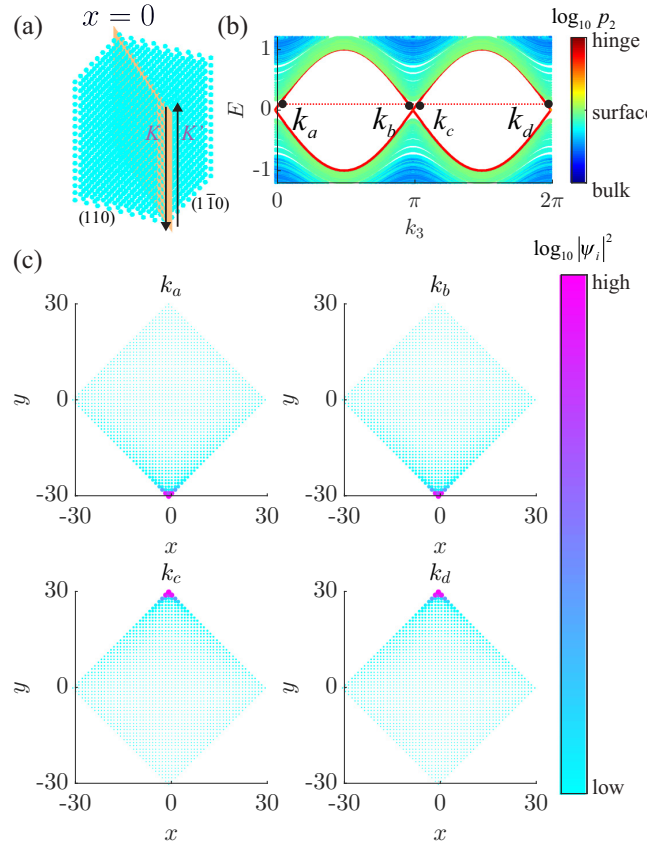

FIG. 1. (a) Schematic plot of a WSOTI. Hinge states (black arrows) of different valleys are antiparallel. The dark yellow plane is $x = 0$. (b) Energy spectrum $E(k_3)$ of Eq. (1) for $M = t, B = 0.2t$. Colors encode $\log_{10} p_2$. Red dotted line locates $E = 0.02t$. (b) Spatial distribution of the in-gap helical states $k_3 = k_{a,b,c,d}$ shown in (b). Colors encode $\log_{10}|\psi_i|^2$.

widely used to describe quantum spin Hall systems, e.g., HgTe/CdTe quantum well, where the helical states come in Kramer pairs with spin-momentum locked [4]. Analogously, we expect helical states appear on the plane of $x = 0$ as well but with a *valley-momentum locked*, i.e., electrons in hinge channels that behave as massless relativistic particles with a given valley pseudospin is locked to its propagating direction, see Fig. 1(a).

Figure 1(b) shows the energy spectrum $E(k_3)$ of model (1) on a rectangle sample of size $L_\parallel/\sqrt{2}\times L_\parallel/\sqrt{2}\times L_\perp$ with periodic boundary condition (PBC) in the z direction and OBCs on surfaces perpendicular to (110) and $(1\bar{1}0)$. Colors in Fig. 1(b) encode the common logarithmic of participation ratio, defined as $\mathcal{P}_2(E) = 1/\sum_{\boldsymbol{i}}|\psi_{\boldsymbol{i}}(E)|^4$. Here $|\psi_{\boldsymbol{i}}(E)|$ is the normalized wave function amplitude of energy E at site $\boldsymbol{i}$. $\mathcal{P}_2$ measures the number of sites occupied by state of E [43–45] and allows one to distinguish hinge states from the bulk and surface states easily. Clearly, for $M = t$ and $B = 0.2t$, two pairs of gapless hinge modes appear. Those near $k_3 = 0$ ($k_3 = \pi$) are described by the up (down) block of Eq. (2), see Appendix B. Wave function distributions of four specific hinge states $k_{a,b,c,d}$ of energy $E = 0.02t$ are shown in Fig. 1(c). States of k_a and k_b (k_c and k_d), respectively,

propagating along $\pm z$ directions, are localized on the same hinge $x = 0, y = L_\parallel/2$ ($x = 0, y = -L_\parallel/2$).

In quantum spin Hall systems where spin s_z is a good quantum number, spin-Chern numbers play the role of topological invariant. Similarly, we employ the valley-Chern number C_{valley} to measure the topology of the surface states in the clean limit that tells the emergence of helical hinge states. C_{valley}, widely used in layered-graphene systems by studying the valley Hall effect [46–48], is defined as

$$C_{\text{valley}} = C_{\boldsymbol{K}} - C_{\boldsymbol{K}'} \tag{3}$$

with $C_{\boldsymbol{K}}$ and $C_{\boldsymbol{K}'}$ being the valley-Chern number for $\boldsymbol{K}$ and $\boldsymbol{K}'$, respectively. The summation of the Berry curvature over all occupied states of electrons in a valley η_i gives $C_{\eta_i} = \eta_i \text{sgn}[B]/2 = \pm 1/2$, see Appendix C for more details. Thus, the valley-Chern number is quantized to 1.

We would like to discuss the material relevance of the predicted WSOTI before moving further. The WSOTI is a direct consequence of the band inversion of surface states of WFOTIs. Remarkably, a recent experiment verified the emergency of WFOTI phase in quasi-one-dimensional bismuth iodide with the same $\mathbb{Z}_2$ index studied here [49,50]. Besides, it is found that band inversion of surface states can happen in bismuth with respect to certain crystal symmetries [34,35]. We thus expect bismuth is an ideal material to search for the helical hinge states. Rather than electronic systems, WSOTIs may be also found in other systems like photons, where the WFOTI has already been visualized [51] and a band inversion can be artificially induced in principle.

III. STABILITY AGAINST DISORDERS

To study the robustness of the helical hinge states against disorders, we add a random onsite potential $V = \sum_i c_i^\dagger v_i I_4 c_i$ to the lattice model of Hamiltonian Eq. (1), where $c_i^\dagger$ (c_i) is the electron creation (annihilation) operator at site $\boldsymbol{i}$. v_i distributes randomly in the range of $[-W/2, W/2]$. Disorders break the lattice translational symmetry so that C_{valley} is not good anymore. Yet, we can still use the $L_\parallel = L_\perp = L$ dependence of $\eta_{W,L}(E) = \langle \sum_{i\in\text{Hinge}} |\psi_{i,E}(W,L)|^2 \rangle$ to characterize hinge states, where the sum is over all the lattice sites on two hinges of $x = 0, y = \pm L/2$ and $\langle \cdots \rangle$ denotes ensemble average. $\eta_{W,L}(E)$ measures the distribution on the hinges. Naturally, for states with dominated occupation probability on hinges, $\eta_{W,L}(E)$ approaches a finite value for $L \gg 1$, while for surface and bulk states, $\eta_{W,L}(E)$ should decrease with L algebraically.

Let us focus on $E = 0$. Numerically, we use the retarded Lanczos method to find the eigenfunction of the nearest level around $E = 0$ of the disordered bar and calculate $\eta_{W,L}$ and $\zeta_{W,L}$ accordingly. In our scenario, we first use the KWANT package [52] to construct a Hamiltonian matrix H out of tight-binding model Eq. (1). We then solve the eigenequation $H\psi = E\psi$ using the SCIPY library [53] to obtain the required eigenenergies and eigenfunctions. In Fig. 2(a), we display $\eta_{W,L}$ as a function of W for various L [52,53]. Apparently, there exists a critical disorder $W_{c1}/t \simeq 1.2 \pm 0.2$ below which all curves merge and form a plateau at $\eta_{W,L} \simeq 0.65$, see the orange line. Mergence and plateau of $\eta_{W,L}$ are strong indications of helical hinge states at a finite disorder. For $W > W_{c1}$,

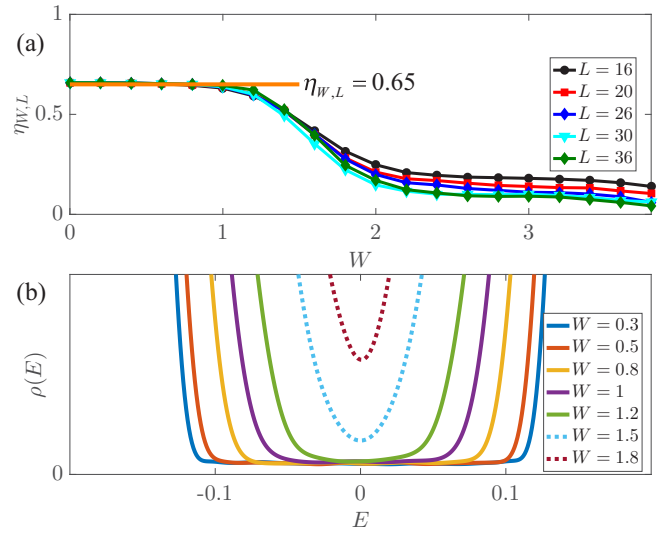

FIG. 2. (a) $\eta_{W,L}$ as a function of W for various L. Each data is averaged over more than 100 samples. (b) $\rho(E)$ for $L = 200$ and various W: solid (dash) lines are for $W < W_{c1}$ ($W > W_{c1}$). Here, $M = t$, $B = 0.2t$, and $L_\parallel = L_\perp = L$.

$\eta_{W,L}$ decreases with L. As shown below, they are surface states for $W > W_{c1}$, featured by a finite size-independent occupation probability on surfaces as $L \to \infty$.

More insights can be obtained by investigating how disorders affect the gap of surface states through the self-consistent Born approximation (SCBA) [54–56], where the self-energy is given by

$$\Sigma = W^2/(48\pi^2) \int_{\text{BZ}} [(E + i0)I_4 - h_{\text{surface}}(\boldsymbol{p}_\parallel) - \Sigma]^{-1} d\boldsymbol{p}_\parallel. \tag{4}$$

We write Σ as $\Sigma = \Sigma_0 I_4 + \sum_{\mu=1}^5 \Sigma_\mu \gamma^\mu$ with $\gamma^{1,2,3,4,5} = (\tau_1 \otimes I_2, \tau_3 \otimes I_2, \tau_2 \otimes \sigma_3, \tau_2 \otimes \sigma_3, \tau_1 \otimes \sigma_3, \tau_3 \otimes \sigma_3)$. For E=0, $\Sigma_{1,3,4,5} = 0$ and Σ_0 is a pure imaginary number, i.e., $\Sigma_0 = i(-1/\tau)$. Then, we obtain (see Appendix D)

$$\frac{1}{\tau} = \frac{1}{\tau} \frac{W^2}{48\pi^2 t^2} \int_{\text{BZ}} \frac{d\boldsymbol{p}_\parallel}{p_2^2 + p_3^2 + \left(\tilde{B} - p_2^2/4\right)^2 - 1/\tau^2}, \tag{5}$$

where the Dirac mass is renormalized as $\tilde{B} = B + \Sigma_2$. Here, τ is the lifetime of the zero-energy surface states, i.e., $\rho_{\text{surface}}(E = 0) \propto 1/\tau$. For $W < W_{c1}$, $1/\tau = 0$ and surface states are gapped at $E = 0$, while for $W > W_{c1}$, finite τ solutions are allowed and $\rho_{\text{surface}}(E = 0) \neq 0$. Thus, with increasing W, we expect the WSOTI undergoes a gap-closing transition at the critical disorder W_{c1} whose approximate solution is determined from Eq. (5) with $\tilde{B} = B$ is $W_{c1} = t(24\pi/(\ln[16\sqrt{2}/B]))^{1/2}$. The closed-form solution indicates that W_{c1} increases with B, which measures the width of the surface gap, and explains qualitatively Fig. 2(a).

Dispersion relation of the hinge states in the clean limit is linear in p_3 near two valleys (see Appendix B). Since disorders do not change the linear dispersion relation within the framework of SCBA, we expect a constant density of helical hinge states for $|E| < \Delta_1$ with Δ_1 being the gap of surface states for $W < W_{c1}$. This behavior is confirmed by numerical calculations of the average density of states (DOS),

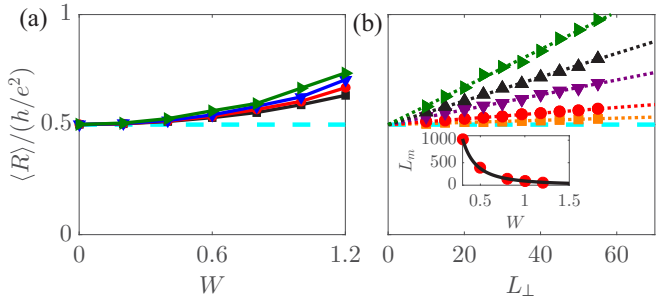

FIG. 3. (a) $\langle R\rangle$ as a function of W for $L_\perp = L_\parallel = L = 16, 20, 24, 32$ (from down to up). (b) $\langle R\rangle$ versus $L_\perp$ for $W/t = 0.3, 0.5, 1, 0.8, 1.2$ (from down to up) and $L_\parallel = 10$. Dotted lines are fitted by Eq. (6). Inset: The obtained L_m as a function W. Black solid line is a fit of $L_m = ct^2/W^2$ with $c = 92$. Cyan dashed lines locate the intrinsic resistance $h/(2C_{\text{valley}}e^2)$. Here, $M = t$ and $B = 0.2t$. Each data point is averaged over 1000 samples.

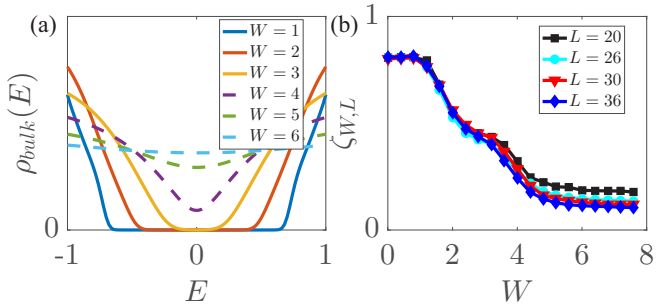

FIG. 4. (a) $\rho_{\text{bulk}}(E)$ for various $W > W_{c1}$ and $L = L_\parallel = L_\perp = 200$. Solid (dashed) lines are for $W < W_{c2}$ ($W > W_{c2}$). (b) $\zeta_{W,L}$ versus W for various $L = L_\parallel = L_\perp$. Here, $M = t$ and $B = 0.2t$.

defined as $\rho(E) = \langle(\sum_{q=1}^{8L^3}\delta(E - E_q))\rangle/(8L^3)$ with E_q being the eigenvalues of the systems. We calculate $\rho(E)$ through the kernel polynomial method [57] and plot those for $L = 200$ and various W/t from 0.3 to 1.8 in Fig. 2(b). The average $\rho(E)$ of the disordered bar of $L = 200$ for various W that are obtained from 10 ensembles with 1024 Chebyshev moments. Indeed, $\rho(E)$ is independent of W and E within $|E| < \Delta_1$ and $W < W_{c1}$, while Δ_1 decreases with W. For $W > W_{c1} \simeq 1.2t$, the constant $\rho(E)$ fades, and $\rho(E = 0)$ increases with W. Hence, the constant DOS can be another fingerprint of the helical hinge states, akin to chiral hinge states [36].

IV. ELECTRONIC TRANSPORT

We have also investigated the electronic transport through helical hinge states by using the Landauer-Büttiker formula to calculate the two-terminal resistance R of the Hall bar connected by two semi-infinite leads along the z direction. The dimensionless resistance of a disordered bar between two clean semi-infinite leads at a given Fermi level E can be calculated by $R = h/(e^2\text{Tr}[TT^\dagger])$ with T being the transmission matrix [58]. We focus on $W < W_{c1}$ and $E = 0$. Figure 3(a) plots the $\langle R\rangle$ versus W for various $L_\parallel = L_\perp = L$. For $W = 0$, R displays a perfect quantum plateau at $h/(2e^2)$. In the presence of disorders, $\langle R\rangle$ notably increases with W and L, even for very small disorders. Furthermore, we investigate how $\langle R\rangle$ depends on system sizes. Figure 3(b) shows $\langle R\rangle$ as a function of $L_\perp$ for various W and a fixed $L_\parallel$. We find that $\langle R\rangle$ is linearly increased with $L_\perp$ and can be well described by the following formula

$$\langle R\rangle = \frac{h}{e^2}\left(\frac{1}{2C_{\text{valley}}} + \frac{L_\perp}{L_m}\right) \tag{6}$$

with L_m being a characteristic length but independent of $L_\parallel$, see Appendix E. Remarkably, very similar features have also been observed in quantum spin Hall systems with spin dephasings [59].

Equation (6) can be understood as follows. Unlike chiral hinge states, helical hinge states always suffer from the intervalley scattering caused by short-range disorders such that the resistance plateau at $W = 0$ are destroyed. Indeed, one can treat Eq. (6) as a combination of an intrinsic resistance $h/(2C_{\text{valley}}e^2)$ coming from the nontrivial topology of surface states and an extrinsic resistance due to the intervalley scattering. The latter should be proportional to $L_\perp$ and independent of $L_\parallel$, while L_m is a length acting like mean free length, i.e., $L_m \sim v_g\tau_m$ with $1/\tau_m$ being the intervalley scattering rate and v_g being the group velocity. Through Fermi's golden rule, we obtain $L_m \sim t^2/W^2$ (see Appendix E), which accords well with numerical data, as shown in the inset of Fig. 3(b).

V. STRONG DISORDERS

To have a complete picture, we study the fate of WSOTIs under stronger disorders. For $W > W_{c1}$, the surface energy gap Δ_1 is closed while the bulk energy gap Δ_2 remains finite. The system becomes a WFOTI. The conclusion is confirmed by demonstrating that the mid-bulk-gap states are localized on the surfaces. Akin to WSOTIs, WFOTIs survive up to a higher disorder W_{c2} at which $\Delta_2 = 0$ and the system transforms into a DM beyond W_{c2}. Figure 4(a) shows the calculated density of bulk states $\rho_{\text{bulk}}(E)$, obtained by applying with PBCs on all directions so that no surface and hinge states are allowed, for various disorders $W > W_{c1}$. Clearly, there is always a finite bulk gap for $W < W_{c2} \simeq 3t$. Also, these results demonstrate that the nonzero $\rho(E)$ around $E = 0$ for $W > W_{c1}$ shown in Fig. 2(b) is from the contributions of surface states.

Stronger evidence of the WFOTI-DM transition is given in Fig. 4(b), which displays $\zeta_{W,L} = \langle\sum_{i\in\text{Surface}}|\psi_{i,E=0}(W,L)|^2\rangle$ as a function of W for various $L_\parallel = L_\perp = L$. One should not confuse $\zeta_{W,L}$, the distribution of state $E = 0$ on surfaces, with $\eta_{W,L}$, the distribution on hinges. The identification of the nature of state $E = 0$ thus can be guided by the following observations: (1) For hinge and surface states, $\zeta_{W,L}$ proceeds toward a finite constant in $L \to \infty$. (2) For bulk states, $\zeta_{W,L}$ decreases with L and scales with L as $1/L$ for large enough systems. Following such criteria, we determine $W_{c2} \simeq 3t$ such that the system is a WFOTI for $W_{c2} > W \geqslant W_{c1}$, while it becomes a DM for $W \geqslant W_{c2}$.

Anderson localization occurs at extremely strong disorders $W_{c3} > W_{c2}$, and the system becomes an insulator for $W > W_{c3}$. The Anderson localization transition from a diffusive metal to an Anderson insulator at a large disorder W_{c3} is investigated through the finite-size scaling analysis of the PR $\mathcal{P}_2(W, L)$ for a given disorder W and a system size $L_\parallel = L_\perp = L$. Near W_{c3},

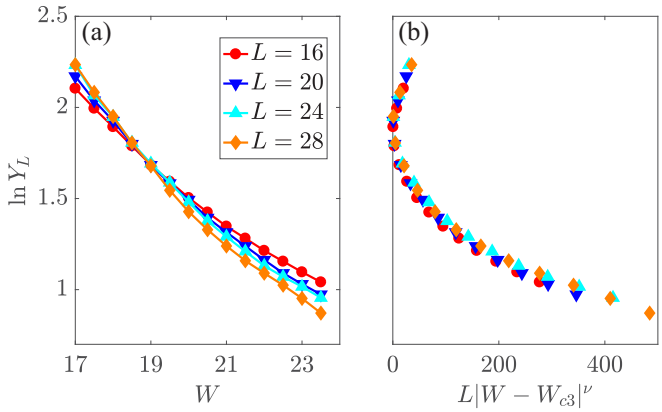

FIG. 5. (a) $\ln Y_L$ as a function of W for $M = t$ and $B = 0.2t$. (b) Scaling function $\ln Y_L = \ln f(L|W - W_{c3}|^{\nu})$.

PR follows the one-parameter scaling function

$$\mathcal{P}_2(W, L) = L^D[f(L/\xi) + CL^{-y}]. \tag{7}$$

Here, D is the fractal dimension, ξ is the correlation length and diverges as $\xi \propto |W - W_{c3}|^{-\nu}$ with ν being the critical exponent characterized the universality of Anderson localization transition. y is the exponent of the irrelevant scaling variable, C is a constant, and $f(x)$ is the unknown scaling function.

To study such a transition, we introduce a quantity $Y_L(W) = \mathcal{P}_2 L^{-D} - CL^{-y}$. The recognition of the critical disorder is guided by the following observations: (1) For DMs (AIs), $Y_L(W)$ increases (decreases) with L. (2) At the critical disorder, $Y_L(W)$ is independent of L. (3) Near the critical disorders, $Y_L(W)$ is the scaling function $f(x = L/\xi)$ with $\xi \propto |W - W_{c3}|^{\nu}$. By following the approach demonstrated in Ref. [60], we perform a chi-square fit of the numerically calculated $\mathcal{P}_2(W, L)$ by Eq. (7) and obtain $W_{c3}/t = 18 \pm 1$, $\nu = 1.7 \pm 0.3$, $y = 0.9 \pm 0.2$, and $C = 0.9 \pm 0.1$. The goodness-of-fit is $Q = 10^{-2}$, indicating the fitting is acceptable [61]. We then plot $\ln Y_L$ as a function of W in Fig. 5(a), where curves for different L merge at a single point W_{c3}. The unknown scaling function is also obtained, see Fig. 5(b). There are two bundles in Fig. 5(b) with the upper (lower) standing for diffusive metals (Anderson insulators). The obtained critical exponent ν is closed to that of the Gaussian unitary ensemble established before [36,62].

VI. CONCLUSION

In short, we have theoretically demonstrated the genuineness of WSOTIs with valley-momentum locked helical hinge states. Such hinge states are featured by the quantized valley-Chern number in the clean limit and are robust against disorders until the band gap of surface states collapses. However, the normal quantized conductance of 1D channel is destroyed by disorders. With further increasing disorder, quantum transitions from WSOTI to WFOTI and from WFOTI to DM happen in order. At very strong disorders, the system becomes an insulator through the Anderson localization transition.

ACKNOWLEDGMENTS

This work is supported by the National Natural Science Foundation of China (Grants No. 11774296, No. 11704061, and No. 11974296) and Hong Kong RGC (Grants No. 16301518 and No. 16301619). C.W. acknowledges the kind help from Jie Lu.

APPENDIX A: LOW-ENERGY SURFACE HAMILTONIAN

In Appendix A, we derive the low-energy effective Hamiltonian for the surface states. We first expand Eq. (1) near the Gamma point $\mathbf{\Gamma} = (0, 0, 0)$

$$h_{\text{bulk}}(\boldsymbol{p}) = tp_2\Gamma^1 + \left(\tilde{M} + \frac{t}{2}(p_1^2 + p_1^2)\right)\Gamma^2 + tp_3\Gamma^3 + tp_1\Gamma^4, \tag{A1}$$

where $\boldsymbol{p} = \boldsymbol{k} - \mathbf{\Gamma}$ and $\tilde{M} = M - 2t$. The lattice constant is set to 1. Periodical boundary conditions (PBCs) on y and z directions and the open boundary condition (OBC) in the x direction are assumed first. We split Hamiltonian (A1) into two parts, $h_{\text{bulk}} = h^0_{\text{bulk}} + h^1_{\text{bulk}}$ with

$$h^0_{\text{bulk}}(\partial_x) = -it\partial_x\Gamma^4 + \left(\tilde{M} - \frac{t}{2}\partial_{xx}\right)\Gamma^2 \tag{A2}$$

and

$$h^1_{\text{bulk}}(\boldsymbol{p}_{\parallel}) = tp_2\Gamma^1 + \frac{t}{2}p_2^2\Gamma^2 + tp_3\Gamma^3 + B\Gamma^{31}. \tag{A3}$$

Here $\boldsymbol{p}_{\parallel} = (p_2, p_3)$, $M = t$, and $B = 0.2t$. We treat h^1_{bulk} as a perturbation since $B = 0.2t \ll |\tilde{M}| = t$. We would like to show that the zero-energy solution of $h^0_{\text{bulk}}(\partial_x)$ is topological surface states. To begin, we perform a unitary transformation

$$\tilde{h}^0_{\text{bulk}}(\partial_x) = Uh^0_{\text{bulk}}(\partial_x)U^{-1} \tag{A4}$$

with $U = \exp[i\pi s_1/4] \otimes \exp[-i\pi\sigma_1/4]$ (rotating around the x axis by $\pm\pi/2$ in spin and orbital spaces). $\tilde{h}^0_{\text{bulk}}(\partial_x)$ is easy to solve since it is block diagonalized. Consider the upper block of $\tilde{h}^0_{\text{bulk}}(\partial_x)$ first. For $E = 0$ states, we have

$$\begin{bmatrix} 0 & \tilde{M} - t\partial_{xx}/2 - t\partial_x \\ \tilde{M} - t\partial_{xx}/2 + t\partial_x & 0 \end{bmatrix}\begin{bmatrix}\psi_1 \\ \psi_2\end{bmatrix} = 0. \tag{A5}$$

We choose $\exp[-\lambda x]$ as trial solutions and obtain

$$\begin{aligned}\psi_1 &= d_1\exp[(1+i)x] + d_2\exp[(1-i)x] \\ \psi_2 &= c_1\exp[-(1+i)x] + c_2\exp[-(1-i)x].\end{aligned} \tag{A6}$$

We consider the two opposite surfaces located at $x = L_x/2$ and $x = -L_x/2$ with L_x measuring the distance between two surfaces. The surface state on $x = -L_x/2$ is given by ψ_2. Boundary condition requires that $\psi_2(x = -L_x/2) = 0$, and the zero-energy wave function reads

$$\psi_2 = \psi_- = 2c\exp[-x - L_x/2]\sin[-x - L_x/2]\begin{bmatrix}0\\1\\0\\0\end{bmatrix}, \tag{A7}$$

where c is determined by $\int_{-L_x/2}^{L_x/2}|\psi_-|^2dx=1$,

$$c=\sqrt{\frac{2}{1-\exp[-2L_x](\sin[2L_x]-\cos[2L_x]+2)}}. \tag{A8}$$

Similarly, the surface state on $x=L_x/2$ is given by ψ_1,

$$\psi_1=\psi_+=2c\exp[x-L_x/2]\sin[x-L_x/2]\begin{bmatrix}1\\0\\0\\0\end{bmatrix}. \tag{A9}$$

The subscript $\pm$ denote surface states on $x=\pm L_x/2$, respectively. For the lower block of Eq. (A4), we find two additional zero-energy surface states solutions $\phi_\pm$:

$$\phi_+=2c\exp[x-L_x/2]\sin[x-L_x/2]\begin{bmatrix}0\\0\\0\\1\end{bmatrix} \tag{A10}$$

and

$$\phi_-=2c\exp[-x-L_x/2]\sin[-x-L_x/2]\begin{bmatrix}0\\0\\1\\0\end{bmatrix}. \tag{A11}$$

Having obtained the four zero-energy surface solutions, the effective Hamiltonian in the space spanned by the four surface states is

$$\begin{aligned}h_{\mathbb{S}}(\boldsymbol{p}_\parallel)&=\int\begin{bmatrix}\psi_+^\dagger\\ \phi_+^\dagger\\ \psi_-^\dagger\\ \phi_-^\dagger\end{bmatrix}\left(Uh^1_{\text{bulk}}(\boldsymbol{p}_\parallel)U^{-1}\right)[\psi_+\quad\phi_+\quad\psi_-\quad\phi_-]dx\\&=(tp_2s_1-tp_3s_2+Bs_3)\otimes\sigma_0+\frac{t'}{2}p_2^2s_3\otimes\sigma_1.\end{aligned} \tag{A12}$$

Here,

$$t'=t(2c^2\exp[-L_x](\sin[L_x]-L_x\cos[L_x])). \tag{A13}$$

If the two opposite surfaces are well separated, say $L_x\gg 1$, $t'\simeq 0$ is negligible. However, if the two surfaces meet at the plane of $x=0$ such that $L_x\simeq 0$, $t'=t/2$. In this case, hinge states emerge if OBCs are applied in the y direction. To obtain a clearer picture, we further perform a unitary transformation to Eq. (A12) with $U'=\exp[-i\pi s_1/4]\otimes\exp[i\pi\sigma_2/4]$:

$$\tilde{h}_{\mathbb{S}}(\boldsymbol{p}_\parallel)=U'h_{\mathbb{S}}(\boldsymbol{p}_\parallel)U'^{-1}. \tag{A14}$$

$\tilde{h}_{\mathbb{S}}(\boldsymbol{p}_\parallel)$ is now block diagonalized with the upper and the lower blocks being $tp_2\tau_1+tp_3\tau_3+(B+t'p_2^2/2)\tau_2$ and $tp_2\tau_1+tp_3\tau_3+(B-t'p_2^2/2)\tau_2$, respectively. Here, $\tau_{1,2,3}$ are the Pauli matrices acting on the subspaces $\{|-\psi_++i\phi_++\psi_--i\phi_-\rangle, |i\psi_+-\phi_+-i\psi_-+\phi_-\rangle\}$. Since band inversion can only happen on the lower block of $\tilde{h}_{\mathbb{S}}(\boldsymbol{p}_\parallel)$ for $B=0.2t>0$. We thus ignore the upper block and keep the lower block only:

$$h_{\mathbb{S}}(\boldsymbol{p}_\parallel)=tp_2\tau_1+tp_3\tau_3+\left(B-t'p_2^2/2\right)\tau_2. \tag{A15}$$

Likewise, we can find the effective Hamiltonian of the surface states near $\boldsymbol{R}=(\pi,\pi,\pi)$ reads

$$\mathcal{T}h_{\mathbb{S}}(\boldsymbol{p}_\parallel)\mathcal{T}^{-1}=tp_2\tau_1+tp_3\tau_3-\left(B-t'p_2^2/2\right)\tau_2, \tag{A16}$$

where we introduce a pseudo-time-reversal symmetry operator $\mathcal{T}=-i\tau_2K$ with K being the complex conjugate. The total effective Hamiltonian thus reads

$$h_{\text{surface}}(\boldsymbol{p}_\parallel)=\begin{bmatrix}h_{\mathbb{S}}(\boldsymbol{p}_\parallel) & 0\\ 0 & \mathcal{T}h_{\mathbb{S}}(\boldsymbol{p}_\parallel)\mathcal{T}^{-1}\end{bmatrix}, \tag{A17}$$

where the upper and lower blocks refer to valleys $\boldsymbol{K}=(0,0)$ and $\boldsymbol{K}'=(\pi,\pi)$, respectively.

APPENDIX B: LOW-ENERGY HAMILTONIAN OF HELICAL HINGE STATES

In Appendix B, we show the existence of helical hinge states, which locate on the boundary of two surfaces intersected on the plane of $x=0$. At this stage, we apply OBCs in the y direction to Eq. (A17) and keep the PBC in the z direction such that p_3 is still a good quantum number. We consider two boundary surface $(x,y)=(0,L_\parallel/2)$, $(0,-L_\parallel/2)$ and replace p_2 by $-i\partial_y$. Consider the upper block of Eq. (A17) first. Again, we split it into two parts with $L_x=0$ ($t'=t/2$)

$$h^0_{\mathbb{S}}(\partial_y)=-i\partial_y\tau_1+(B+t\partial_{yy}/4)\tau_2 \tag{B1}$$

and

$$h^1_{\mathbb{S}}(p_3)=tp_3\tau_3. \tag{B2}$$

Similarly, we treat Eq. (B2) as a perturbation and demonstrate that zero-energy solutions of Eq. (B1) are hinge states localized at the two boundaries $(x,y)=(0,L_\parallel/2)$, $(0,-L_\parallel/2)$. For $E=0$, we have

$$\begin{bmatrix}0 & t\partial_y+(B+t\partial_{yy}/4)\\ t\partial_y-(B+t\partial_{yy}/4) & 0\end{bmatrix}\begin{bmatrix}\Psi_1\\ \Psi_2\end{bmatrix}=0. \tag{B3}$$

The equation has solutions of $\exp[-\eta_{1(2)}y]$ with (recall $B/t=0.2$)

$$t\eta_1^2/4+t\eta_1+B=0\rightarrow\eta_{1,\pm}=2(-1\pm\sqrt{1-B/t})<0$$

and

$$t\eta_2^2/4-t\eta_2+B=0\rightarrow\eta_{2,\pm}=2(1\pm\sqrt{1-B/t})>0.$$

Then,

$$\begin{aligned}\Psi_1&=f_1\exp[-\eta_{1,+}y]+f_2\exp[-\eta_{1,-}y]\\ \Psi_2&=e_1\exp[-\eta_{2,+}y]+e_2\exp[-\eta_{2,-}y].\end{aligned} \tag{B4}$$

The hinge state localized at $(x,y)=(0,-L_\parallel/2)$ is given by Ψ_2, and boundary condition $\Psi_2(y=-L_\parallel/2)=0$ requires that

$$\frac{e_1}{e_2}=\frac{\exp[\eta_{2,-}L_\parallel/2]}{-\exp[\eta_{2,+}L_\parallel/2]}, \tag{B5}$$

and normalization condition requires that

$$e=\frac{1}{\exp[(\eta_{2,+}+\eta_{2,-})L_\parallel/2]}\sqrt{\frac{2(\eta_{2,+}+\eta_{2,-})\eta_{2,+}\eta_{2,-}}{(\eta_{2,+}-\eta_{2,-})^2}}, \tag{B6}$$

where we have assumed that $L_\parallel\gg 1$. Then, the hinge state

solution reads

$$\Psi_{0,-L_\parallel/2} = \sqrt{\frac{8B}{t-B}}\exp[-2(y+L_\parallel/2)] \times \sinh\left[-2\sqrt{1-\frac{B}{t}}(y+L_\parallel/2)\right]\begin{bmatrix}0\\1\\0\\0\end{bmatrix}. \quad \text{(B7)}$$

For the hinge states localized at $(x, y) = (0, L_\parallel/2)$ (given by Ψ_1), we obtain

$$\Psi_{0,L_\parallel/2} = \sqrt{\frac{8B}{t-B}}\exp[2(y-L_\parallel/2)] \times \sinh[-2\sqrt{1-B/t}(y-L_\parallel/2)]\begin{bmatrix}1\\0\\0\\0\end{bmatrix}. \quad \text{(B8)}$$

Likewise, we can calculate the zero-energy hinge states for the other valley [lower block of Eq. (A17)]

$$\Phi_{0,-L_\parallel/2} = \sqrt{\frac{8B}{t-B}}\exp[-2(y+L_\parallel/2)] \times \sinh\left[-2\sqrt{1-\frac{B}{t}}(y+L_\parallel/2)\right]\begin{bmatrix}0\\0\\1\\0\end{bmatrix} \quad \text{(B9)}$$

and

$$\Phi_{0,L_\parallel/2} = \sqrt{\frac{8B}{t-B}}\exp[2(y-L_\parallel/2)] \times \sinh\left[-2\sqrt{1-\frac{B}{t}}(y-L_\parallel/2)\right]\begin{bmatrix}0\\0\\0\\1\end{bmatrix}. \quad \text{(B10)}$$

Since we have obtained the four zero-energy hinge states solutions [Eqs. (B7)–(B10)], the effective Hamiltonian spanned by these states is

$$h_{\text{hinge}}(p_3) = \begin{bmatrix} tp_3 & 0 & 0 & 0\\ 0 & -tp_3 & 0 & 0\\ 0 & 0 & -tp_3 & 0\\ 0 & 0 & 0 & tp_3\end{bmatrix}. \quad \text{(B11)}$$

APPENDIX C: VALLEY-CHERN NUMBER

The quantized valley-Chern number can be used to characterize helical hinge states in the clean limit. In the continuous limit, the Chern number for a given valley η_i reads [46]

$$C_{\eta_i} = \frac{1}{2\pi}\int d\Omega(\boldsymbol{p}_\parallel, \eta_i). \quad \text{(C1)}$$

Note that the Hamiltonian of surface states Eq. (2) of a given valley can be written as $\boldsymbol{h}\cdot\boldsymbol{\tau}$ with $\boldsymbol{h} = (h_i, h_j, h_k)$ being a real vector. Therefore, the Berry curvature takes the following form [63]:

$$d\Omega(\boldsymbol{p}_\parallel, \eta_i) = \tfrac{1}{4}\epsilon^{ijk}|\boldsymbol{h}|^{-3}h_i dh_j dh_k. \quad \text{(C2)}$$

Here, ϵ^{ijk} is the Levi-Civita symbol. As $\boldsymbol{h}(\boldsymbol{p}_\parallel)$ is a function of $\boldsymbol{p}_\parallel$, $dh_j = (\partial_{p_\alpha}h_j)dp_\alpha$ with $\alpha = 2, 3$. Then,

$$\Omega(\boldsymbol{p}_\parallel, \eta_i) = \frac{1}{2|\boldsymbol{h}|^3}\boldsymbol{h}\cdot\left(\frac{\partial\boldsymbol{h}}{\partial p_2}\times\frac{\partial\boldsymbol{h}}{\partial p_3}\right)dp_2dp_3. \quad \text{(C3)}$$

We can write $\boldsymbol{h} \simeq (tp_2, \eta_i B, tp_3)$ since the Berry curvature are strongly peaked at the valleys where $|\boldsymbol{p}| = 0$. Then, the Chern number of a single valley is

$$C_{\eta_i} = \frac{1}{4\pi}\int_0^{2\pi}\int_0^{+\infty}\frac{-\eta_i Bt^2 pdpd\theta}{(t^2p^2+B^2)^{3/2}}dpd\theta = \frac{\eta_i \text{sgn}[B]}{2}, \quad \text{(C4)}$$

with sgn[x] being the sign function. Therefore, the total valley-Chern number, defined as $C_{\eta_i=1} - C_{\eta_i=-1}$, is thus quantized at 1.

APPENDIX D: CLOSED-FORM SOLUTION OF CRITICAL DISORDERS

In Appendix D, we derive a closed form of W_{c1}. Within the framework of self-consistent Born approximation, the self-energy satisfies [55]

$$\Sigma = \frac{W^2}{48\pi^2}\int\frac{1}{(E_F+i0)I_4 - h_S(\boldsymbol{p}_\parallel) - \Sigma}d\boldsymbol{p}_\parallel, \quad \text{(D1)}$$

where $h_S(\boldsymbol{p}_\parallel)$, the up block of Eq. (A17), is

$$h_S(\boldsymbol{p}_\parallel) = tp_2\gamma^1 + tp_3\gamma^2 + \left(B - \frac{t'}{2}p_2^2\right)\gamma^3. \quad \text{(D2)}$$

Here the five gamma matrices are defined as $\gamma^{1,2,3,4,5} = (\tau_1\otimes I_2, \tau_3\otimes I_2, \tau_2\otimes\tilde{\sigma}_3, \tau_1\otimes\tilde{\sigma}_3, \tau_3\otimes\tilde{\sigma}_3)$ with $\tilde{\sigma}_{1,2,3}$ being the Pauli matrices acting on the valley subspace. I_2 and I_4 are the two-by-two and four-by-four identity matrices, respectively. The self-energy can be written as $\Sigma = \Sigma_0 I_4 + \sum_\mu \Sigma_\mu\gamma^\mu$, i.e.,

$$\Sigma_0 = -\frac{W^2}{48\pi^2}\int\frac{E_F+i0-\Sigma_0}{A(\boldsymbol{p}_\parallel)}d\boldsymbol{p}_\parallel, \quad \text{(D3)}$$

$$\Sigma_1 = \frac{W^2}{48\pi^2}\int\frac{tp_2+\Sigma_1}{A(\boldsymbol{p}_\parallel)}d\boldsymbol{p}_\parallel, \quad \text{(D4)}$$

$$\Sigma_2 = \frac{W^2}{48\pi^2}\int\frac{tp_3+\Sigma_2}{A(\boldsymbol{p}_\parallel)}d\boldsymbol{p}_\parallel, \quad \text{(D5)}$$

$$\Sigma_3 = \frac{W^2}{48\pi^2}\int\frac{B+\Sigma_3-t'p_2^2/2}{A(\boldsymbol{p}_\parallel)}d\boldsymbol{p}_\parallel, \quad \text{(D6)}$$

and $\Sigma_{4,5} = 0$. Here $A(\boldsymbol{p}_\parallel) = (tp_2+\Sigma_1)^2 + (tp_3+\Sigma_2)^2 + (B+\Sigma_3-t'p_2^2/2)^2 - (E_F+i0-\Sigma_0)^2$. It is easy to find that $\Sigma_{1,2} = 0$ since $A(\boldsymbol{p}_\parallel) = A(-\boldsymbol{p}_\parallel)$, while B is normalized by disorders as $\tilde{B} = B + \Sigma_3$. On the other hand, the density of states which relates to the imaginary part of Σ_0 is affected by disorders as well. For $E_F = 0$, Σ_0 is a pure imaginary number, i.e., $\Sigma_0 = i(-1/\tau)$, with τ being given by

$$\frac{1}{\tau} = \frac{1}{\tau}\frac{W^2}{48\pi^2}\int\frac{1}{t^2p_2^2+t^2p_3^2+\left(\tilde{B}-t'p_2^2/2\right)^2-1/\tau^2}d\boldsymbol{p}_\parallel. \quad \text{(D7)}$$

Equation (D7) indicates that there exists a disorder strength W_{c1} below (above) which the density of zero-energy states is

zero (nonzero), i.e., $1/\tau = 0$ ($1/\tau \neq 0$). The critical disorder can be determined by

$$1 = \frac{W_{c1}^2}{48\pi^2}\int \frac{1}{t^2 p_2^2 + t^2 p_3^2 + \left(\tilde{B} - t' p_2^2/2\right)^2} d\boldsymbol{p}_{\parallel}. \tag{D8}$$

Equation (D8) is known as the *gap equation* [55]. To obtain a closed-form solution of W_{c1}, we take the limit $\tilde{B} \to B$ and $L_x \to 0$ ($t' = t/2$) in the right-hand side of Eq. (D8) and write $p_2 = p\cos\theta$ and $p_3 = p\sin\theta$. Then,

$$\frac{48\pi^2 t^2}{W_{c1}^2} = \iint \frac{p\,dp\,d\theta}{(\cos^4\theta/16)p^4 + (1 - B\cos^2\theta/(2t))p^2 + (B/t)^2}. \tag{D9}$$

For $B/t \ll 1$, the integral is

$$\int_0^{2\pi}\int_0^{\infty} \frac{p\,dp}{(\cos^4\theta/16)p^4 + (1 - B\cos^2\theta/(2t))p^2 + (B/t)^2} d\theta \simeq \frac{1}{2}\int_0^{2\pi} \ln\left[\frac{16}{B^2\cos^4\theta/t^2}\right] d\theta \simeq 2\pi \ln\left[\frac{16}{B/t}\right], \tag{D10}$$

and W_{c1} is

$$\frac{W_{c1}}{t} = \sqrt{\frac{24\pi}{\ln[16t/B]}}. \tag{D11}$$

APPENDIX E: MEAN FREE PATH OF ELECTRON IN HELICAL HINGE STATES

In Appendix E, we calculate the mean free path of electron in the helical hinge states. We consider state $\Psi_{0,L_\parallel}$ [given by Eq. (B8)] on the hinge passing through $(x, y) = (0, L_\parallel/2)$. Electrons in the channel propagate along the z direction as shown in Eq. (B11). Let $\Upsilon_{\Psi_{0,L_\parallel}}$ be the total scattering rate of an electron in $\Psi_{0,L_\parallel}$:

$$\Upsilon_{\Psi_{0,L_\parallel}} = \Upsilon_{\Psi_{0,L_\parallel}\to\Psi_{0,-L_\parallel}} + \Upsilon_{\Psi_{0,L_\parallel}\to\Phi_{0,L_\parallel}} + \Upsilon_{\Psi_{0,L_\parallel}\to\Phi_{0,-L_\parallel}}, \tag{E1}$$

where the first term is the intranode scattering and the last two terms are for the internode scattering. The scatting rates are given by the Fermi's golden rule. After some calculations, we find

$$\Upsilon_{\Psi_{0,L_\parallel}\to\Psi_{0,-L_\parallel}} = \frac{1}{\hbar}\frac{W^2B^2L_\parallel^2}{3t(t-B)^2}\exp[-4(1-\sqrt{1-B/t})L_\parallel], \tag{E2}$$

which is the same as $\Upsilon_{\Psi_{0,L_\parallel}\to\Phi_{0,-L_\parallel}}$. To derive Eq. (E2), we have assumed that the energy dispersion of hinge states is linear in p_3 even in the presence of weak disorders. This is consistent with the numerically obtained DOS shown in Fig. 2(b). We can define a typical length scale

$$l_0 = 1/(4(1-\sqrt{1-B/t})) \tag{E3}$$

such that

$$\Upsilon_{\Psi_{0,L_\parallel}\to\Psi_{0,-L_\parallel}} = \Upsilon_{\Psi_{0,L_\parallel}\to\Phi_{0,-L_\parallel}} \sim \exp[-L_\parallel/l_0]. \tag{E4}$$

Thus, the scattering from $\Psi_{0,L_\parallel}$ to $\Psi_{0,-L_\parallel}$ and $\Phi_{0,L_-\parallel}$ can be ignored if $L_\parallel \gg l_0$. In general, the system length considered in this work is much larger than $l_0 \simeq 2$ for $B/t = 0.2$. Therefore, $\Upsilon_{\Psi_{0,L_\parallel}\to\Psi_{0,-L_\parallel}} = \Upsilon_{\Psi_{0,L_\parallel}\to\Phi_{0,-L_\parallel}} = 0$.

On the other hand, for the scattering from $\Psi_{0,L_\parallel}$ to $\Phi_{0,L_\parallel}$ which is localized at the same hinge, we have

$$\overline{|\langle\Psi_{0,L_\parallel}|V|\Phi_{0,L_\parallel}\rangle|^2} = \frac{W^2 a}{12L_\perp}. \tag{E5}$$

Then, the total scattering rate in the limit of $L_\parallel \gg l_0$ thus reads

$$\frac{1}{\tau_m} = \Upsilon_{\Psi_{0,L_\parallel}} = \Upsilon_{\Psi_{0,L_\parallel}\to\Phi_{0,L_\parallel}} = \frac{W^2}{12\hbar t}. \tag{E6}$$

On the other hand, the group velocity of electrons in the hinge channel $\Psi_{0,L_\parallel}$ reads

$$v_g = \frac{1}{\hbar}\frac{d(tp_3)}{dp_3} \simeq \frac{t}{\hbar}. \tag{E7}$$

Therefore, the mean free path L_m is

$$L_m \sim |v_g|\tau_m \sim \frac{t^2}{W^2}. \tag{E8}$$

[1] F. D. M. Haldane, Model for a Quantum Hall Effect without Landau Levels: Condensed-Matter Realization of the "Parity Anomaly," Phys. Rev. Lett. **61**, 2015 (1988).

[2] C. L. Kane and E. J. Mele, Z_2 Topological Order and the Quantum Spin Hall Effect, Phys. Rev. Lett. **95**, 146802 (2005).

[3] C. L. Kane and E. J. Mele, Quantum Spin Hall Effect in Graphene, Phys. Rev. Lett. **95**, 226801 (2005).

[4] B. A. Bernevig, T. L. Hughes, and S.-C. Zhang, Quantum spin hall effect and topological phase transition in HgTe quantum wells, Science **314**, 1757 (2006).

[5] M. König, S. Wiedmann, C. Bröune, A. Roth, H. Buhmann, L. W. Molenkamp, X.-L. Qi, and S.-C. Zhang, Quantum spin hall insulator state in HgTe quantum wells, Science **318**, 766 (2007).

[6] A. Roth, C. Brüne, H. Buhmann, L. W. Molenkamp, J. Maciejko, X.-L. Qi, and S.-C. Zhang, Nonlocal transport in the quantum spin hall state, Science **325**, 294 (2009).

[7] M. Z. Hasan and C. L. Kane, Colloquium: Topological insulators, Rev. Mod. Phys. **82**, 3045 (2010).

[8] J. E. Moore, The birth of topological insulators, Nature (London) **464**, 194 (2010).

[9] X.-L. Qi and S.-C. Zhang, Topological insulators and superconductors, Rev. Mod. Phys. **83**, 1057 (2011).

[10] C.-Z. Chang, J. Zhang, X. Feng, J. Shen, Z. Zhang, M. Guo, K. Li, Y. Ou, P. Wei, L.-L. Wang, Z.-Q. Ji, Y. Feng, S. Ji, X. Chen, J. Jia, X. Dai, Z. Fang, S.-C. Zhang, K. He, Y. Wang, L. Lu, X.-C. Ma, and Q.-K. Xue, Experimental observation of the quantum anomalous hall effect in a magnetic topological insulator, Science **340**, 167 (2013).

[11] F. Zhang, C. L. Kane, and E. J. Mele, Surface State Magnetization and Chiral Edge States on Topological Insulators, Phys. Rev. Lett. **110**, 046404 (2013).

[12] W. A. Benalcazar, B. A. Bernevig, and T. L. Hughes, Quantized electric multipole insulators, Science **357**, 61 (2017).

[13] Y. Peng, Y. Bao, and F. von Oppen, Boundary Green functions of topological insulators and superconductors, Phys. Rev. B **95**, 235143 (2017).

[14] J. Langbehn, Y. Peng, L. Trifunovic, F. von Oppen, and P. W. Brouwer, Reflection-Symmetric Second-Order Topological Insulators and Superconductors, Phys. Rev. Lett. **119**, 246401 (2017).

[15] Z. Song, Z. Fang, and C. Fang, $(d-2)$-Dimensional Edge States of Rotation Symmetry Protected Topological States, Phys. Rev. Lett. **119**, 246402 (2017).

[16] F. Schindler, A. M. Cook, M. G. Vergniory, Z. Wang, S. S. P. Parkin, B. A. Bernevig, and T. Neupert, Higher-order topological insulators, Sci. Adv. **4**, eaat0346 (2018).

[17] M. Ezawa, Higher-Order Topological Insulators and Semimetals on the Breathing Kagome and Pyrochlore Lattices, Phys. Rev. Lett. **120**, 026801 (2018).

[18] T. Liu, Y.-R. Zhang, Q. Ai, Z. Gong, K. Kawabata, M. Ueda, and F. Nori, Second-Order Topological Phases in Non-Hermitian Systems, Phys. Rev. Lett. **122**, 076801 (2019).

[19] R.-X. Zhang, W. S. Cole, and S. Das Sarma, Helical Hinge Majorana Modes in Iron-Based Superconductors, Phys. Rev. Lett. **122**, 187001 (2019).

[20] Z. Zhang, M. R. Lopez, Y. Cheng, X. Liu, and J. Christensen, Non-Hermitian Sonic Second-Order Topological Insulator, Phys. Rev. Lett. **122**, 195501 (2019).

[21] C. H. Lee, L. Li, and J. Gong, Hybrid Higher-Order Skin-Topological Modes in Nonreciprocal Systems, Phys. Rev. Lett. **123**, 016805 (2019).

[22] R. Queiroz and A. Stern, Splitting the Hinge Mode of Higher-Order Topological Insulators, Phys. Rev. Lett. **123**, 036802 (2019).

[23] X.-W. Luo and C. Zhang, Higher-Order Topological Corner States Induced by Gain and Loss, Phys. Rev. Lett. **123**, 073601 (2019).

[24] D. Varjas, A. Lau, K. Pöyhönen, A. R. Akhmerov, D. I. Pikulin, and I. C. Fulga, Topological Phases without Crystalline Counterparts, Phys. Rev. Lett. **123**, 196401 (2019).

[25] K. Kudo, T. Yoshida, and Y. Hatsugai, Higher-Order Topological Mott Insulators, Phys. Rev. Lett. **123**, 196402 (2019).

[26] H. Chen and X. C. Xie, Interaction-driven topological switch in a $P-$band honeycomb lattice, Phys. Rev. A **100**, 013601 (2019).

[27] H. Araki, T. Mizoguchi, and Y. Hatsugai, Phase diagram of a disordered higher-order topological insulator: A machine learning study, Phys. Rev. B **99**, 085406 (2019).

[28] Z.-X. Li, Y. Cao, P. Yan, and X. R. Wang, Higher-order topological solitonic insulators, npj Comput. Mater. **5**, 107 (2019).

[29] Z. Su, Y. Kang, B. Zhang, Z. Zhang, and H. Jiang, Disorder induced phase transition in magnetic higher-order topological insulator: A machine learning study, Chin. Phys. B **28**, 117301 (2019).

[30] R. Chen, C.-Z. Chen, J.-H. Gao, B. Zhou, and D.-H. Xu, Higher-Order Topological Insulators in Quasicrystals, Phys. Rev. Lett. **124**, 036803 (2020).

[31] A. Agarwala, V. Juričić, and B. Roy, Higher-order topological insulators in amorphous solids, Phys. Rev. Res. **2**, 012067(R) (2020).

[32] A. L. Szabó and B. Roy, Dirty higher-order Dirac semimetal: Quantum criticality and bulk-boundary correspondence, Phys. Rev. Research **2**, 043197 (2020).

[33] R.-X. Zhang, F. Wu, and S. Das Sarma, Möbius Insulator and Higher-Order Topology in $MnBi_{2n}Te_{3n+1}$, Phys. Rev. Lett. **124**, 136407 (2020).

[34] F. Schindler, Z. Wang, M. G. Vergniory, A. M. Cook, A. Murani, S. Sengupta, A. Y. Kasumov, R. Deblock, S. Jeon, I. Drozdov, H. Bouchiat, S. Guéron, A. Yazdani, B. A. Bernevig, and T. Neupert, Higher-order topology in bismuth, Nat. Phys. **14**, 918 (2018)

[35] C. Yue, Y. Xu, Z. Song, H Weng, Y.-M. Lu, C. Fang, and X. Dai, Symmetry-enforced chiral hinge states and surface quantum anomalous Hall effect in the magnetic axion insulator $Bi_{2-x}Sm_xSe_3$, Nat. Phys. **15**, 577 (2019).

[36] C. Wang and X. R. Wang, Disorder-induced quantum phase transitions in three-dimensional second-order topological insulators, Phys. Rev. Research **2**, 033521 (2020).

[37] D. N. Sheng, Z. Y. Weng, L. Sheng, and F. D. M. Haldane, Quantum Spin-Hall Effect and Topologically Invariant Chern Numbers, Phys. Rev. Lett. **97**, 036808 (2006).

[38] J. Li, R.-L. Chu, J. K. Jain, and S.-Q. Shen, Topological Anderson Insulator, Phys. Rev. Lett. **102**, 136806 (2009).

[39] L. Trifunovic and P. W. Brouwer, Higher-Order Bulk-Boundary Correspondence for Topological Crystalline Phases, Phys. Rev. X **9**, 011012 (2019).

[40] L. Fu and C. L. Kane, Topological insulators with inversion symmetry, Phys. Rev. B **76**, 045302 (2007).

[41] C.-K. Chiu, H. Yao, and S. Ryu, Classification of topological insulators and superconductors in the presence of reflection symmetry, Phys. Rev. B **88**, 075142 (2013).

[42] T. Morimoto and A. Furusaki, Topological classification with additional symmetries from Clifford algebras, Phys. Rev. B **88**, 125129 (2013).

[43] X. R. Wang, Y. Shapir, and M. Rubinstein, Analysis of multiscaling structure in diffusion-limited aggregation: A kinetic renormalization-group approach, Phys. Rev. A **39**, 5974 (1989).

[44] C. Wang, Y. Su, Y. Avishai, Y. Meir, and X. R. Wang, Band of Critical States in Anderson Localization in a Strong Magnetic Field with Random Spin-Orbit Scattering, Phys. Rev. Lett. **114**, 096803 (2015).

[45] J. H. Pixley, P. Goswami, and S. Das Sarma, Anderson Localization and the Quantum Phase Diagram of Three Dimensional Disordered Dirac Semimetals, Phys. Rev. Lett. **115**, 076601 (2015).

[46] F. Zhang, J. Jung, G. A. Fiete, Q. Niu, and A. H. MacDonald, Spontaneous Quantum Hall States in Chirally Stacked Few-Layer Graphene Systems, Phys. Rev. Lett. **106**, 156801 (2011)

[47] M. Ezawa, Topological Kirchhoff law and bulk-edge correspondence for valley Chern and spin-valley Chern numbers, Phys. Rev. B **88**, 161406(R) (2013).

[48] F. Zhang, A. H. MacDonaldb, and E. J. Melea, Valley Chern numbers and boundary modes in gapped bilayer graphene, Proc. Natl. Acad. Sci. USA **110**, 10546 (2013).

[49] R. Noguchi, T. Takahashi, K. Kuroda, M. Ochi, T. Shirasawa, M. Sakano, C. Bareille, M. Nakayama, M. D. Watson, K. Yaji *et al.*, A weak topological insulator state in

quasi-onedimensional bismuth iodide, Nature (London) **566**, 518 (2019).

[50] C. Pauly, B. Rasche, K. Koepernik, Marcus Liebmann, M. Pratzer, M. Richter, J. Kellner, M. Eschbach, B. Kaufmann, L. Plucinski *et al.*, Subnanometre-wide electron channels protected by topology, Nat. Phys. **11**, 338 (2015).

[51] Y. Yang, Z. Gao, H. Xue, L. Zhang, M. He, Z. Yang, R. Singh, Y. Chong, B. Zhang, and H. Chen, Realization of a three-dimensional photonic topological insulator, Nature (London) **565**, 622 (2019).

[52] C. W. Groth, M. Wimmer, A. R. Akhmerov, and X. Waintal, Kwant: A software package for quantum transport, New J. Phys. **16**, 063065 (2014).

[53] P. Virtanen, R. Gommers, T. E. Oliphant, M. Haberland, T. Reddy, D. Cournapeau, E. Burovski, P. Peterson, W. Weckesser, J. Bright *et al.*, SciPy 1.0: fundamental algorithms for scientific computing in Python, Nat. Methods **17**, 261 (2020).

[54] C.-Z. Chen, J. Song, H. Jiang, Q.-F. Sun, Z. Wang, and X. C. Xie, Disorder and Metal-Insulator Transitions in Weyl Semimetals, Phys. Rev. Lett. **115**, 246603 (2015).

[55] S. Liu, T. Ohtsuki, and R. Shindou, Effect of Disorder in a Three-Dimensional Layered Chern Insulator, Phys. Rev. Lett. **116**, 066401 (2016).

[56] R. Shindou and S. Murakami, Effects of disorder in three-dimensional Z_2 quantum spin Hall systems, Phys. Rev. B **79**, 045321 (2009).

[57] A. Weiße, G. Wellein, A. Alvermann, and H. Fehske, The kernel polynomial method, Rev. Mod. Phys. **78**, 275 (2006).

[58] A. MacKinnon, The calculation of transport properties and density of states of disordered solids, Z. Phys. B **59**, 385 (1985).

[59] H. Jiang, S. Cheng, Q.-F. Sun, and X. C. Xie, Topological Insulator: A New Quantized Spin Hall Resistance Robust to Dephasing, Phys. Rev. Lett. **103**, 036803 (2009).

[60] W. Chen, C. Wang, Q. Shi, Q. Li, and X. R. Wang, Metal to marginal-metal transition in two-dimensional ferromagnetic electron gases, Phys. Rev. B **100**, 214201 (2019).

[61] W. H. Press, S. A. Teukolsky, W. T. Vetterling, and B. P. Flannery, *Numerical Recipes in Fortran 77*, 2nd ed. (Cambridge University Press, Cambridge, 1996).

[62] T. Kawarabayashi, B. Kramer, and T. Ohtsuki, Anderson transitions in three-dimensional disordered systems with randomly varying magnetic flux, Phys. Rev. B **57**, 11842 (1998).

[63] M. V. Berry, Quantal phase factors accompanying adiabatic changes, Proc. R. Soc. Lond. A **392**, 45 (1984).